Further Modeling of q_{95} Windows for the Suppression of Edge Localized Modes by Resonant Magnetic Perturbations in the DIII-D Tokamak

R. Fitzpatrick [a]

Institute for Fusion Studies, Department of Physics,

University of Texas at Austin, Austin TX, 78712, USA

An improved resonant plasma response model that describes the interaction between a tokamak plasma and a resonant magnetic perturbation (RMP) is developed. The model interpolates between the linear and the nonlinear response regimes, and takes into account the fact that the slip-frequency is non-zero in the nonlinear regime. The improved model is incorporated into the `EPEC` toroidal asymptotic matching code. The modified `EPEC` code is used to investigate RMP-induced edge-localized-mode (ELM) mitigation/suppression in DIII-D H-mode discharge #145380. Allowing for a finite slip-frequency (i.e., relaxing the so-called no-slip constraint) is found to slightly facilitate the locking of driven magnetic island chains to the RMP, and, hence, to slightly facilitate RMP-induced ELM mitigation/suppression. The previously obtained conclusion that the response of a typical H-mode tokamak plasma to an RMP cannot be accurately modeled by linear theory is confirmed. The previously obtained conclusion that the best agreement between theory and observations is achieved by assuming that the natural frequencies of tearing modes, in the absence of the RMP, are determined by the local equilibrium $\mathbf{E}\times\mathbf{B}$ frequency is also confirmed.

[a] rfitzp@farside.ph.utexas.edu

I. INTRODUCTION

In the context of tokamak plasmas, a resonant magnetic perturbation (RMP) refers to an externally generated, (usually) static, helical magnetic perturbation that resonates at one or more "rational" magnetic flux-surfaces within the plasma. Resonant magnetic perturbations have been successfully employed to compensate error fields (i.e., accidentally produced RMPs), and, thereby, to prevent the associated formation of locked modes, in a wide variety of different types of tokamak discharge.[1–3] RMPs have also been successfully used to either mitigate or completely suppress edge-localized-modes (ELMs) in H-mode tokamak discharges.[4–9]

"Asymptotic matching" is by far the most efficient method for modeling the response of a tokamak plasma to an RMP.[10–20] According to the asymptotic matching approach, the response of the plasma to the applied RMP is governed by a combination of flux-freezing and perturbed force balance—this combination is usually referred to as "marginally-stable ideal-magnetohydrodynamics (MHD)"—everywhere in the plasma apart from a number of relatively narrow (in the radial direction) regions in which the applied perturbation resonates with the equilibrium magnetic field. Magnetic reconnection can take place within the resonant regions to produce relatively narrow magnetic island chains. Within the resonant regions, the plasma response is governed by linear or nonlinear two-fluid resistive-MHD, depending on whether the induced magnetic island widths are smaller or larger, respectively, than the corresponding linear layer widths. Thus, when employing the asymptotic matching approach, the equations of marginally-stable ideal-MHD are solved in the so-called "outer region" that comprises most of the plasma (and the surrounding vacuum), the equations of linear/nonlinear two-fluid resistive-MHD are solved in the various resonant layers that constitute the so-called "inner region", and the two sets of solutions are then asymptotically matched to one another.

In the nonlinear resonant response regime, the evolution of the island chain width in a given resonant layer is governed by the familiar "Rutherford island width evolution equation".[12,21] On the other hand, the phase evolution of the island chain is conventionally governed by the well-known "no-slip constraint".[15] According to this constraint, plasma is trapped inside the magnetic separatrix of the island chain, which forces the chain to co-rotate with the local plasma flow. In reality, however, the plasma is able to diffuse resistively

across the separatrix to some extent.[22,23]

The recently developed, toroidal, asymptotic matching code EPEC (Extended Perturbed Equilibrium Code) has been used to simulate RMP-induced ELM mitigation/suppression in DIII-D H-mode plasmas.[24,25] The original EPEC model incorporates the no-slip constraint. The first aim of this paper is to investigate what happens when the no-slip constraint is relaxed in the aforementioned EPEC simulations. The second aim is to examine what happens when an improvement is made to the manner in which the resonant plasma response component of the EPEC model interpolates between the linear and the nonlinear regimes.

II. CYLINDRICAL RESONANT RESPONSE MODEL

A. Introduction

For the sake of simplicity, and also to make a better connection with previous research, let us commence our investigation by discussing the resonant response of a tokamak plasma to an RMP in cylindrical geometry.

B. Plasma Equilibrium

Consider a large aspect-ratio, low-β, tokamak plasma whose magnetic flux-surfaces map out (almost) concentric circles in the poloidal plane. Such a plasma is well approximated as a periodic cylinder. Suppose that the minor radius of the plasma is a. Standard cylindrical coordinates $(r,\, \theta,\, z)$ are adopted. The system is assumed to be periodic in the z-direction, with periodicity length $2\pi\, R_0$, where $R_0 \gg a$ is the simulated plasma major radius. It is convenient to define the simulated toroidal angle $\phi = z/R_0$.

The equilibrium magnetic field is written $\mathbf{B} = [0, B_\theta(r), B_\phi]$. The associated equilibrium plasma current density takes the form $\mathbf{j} = [0, 0, j_\phi(r)]$, where $\mu_0\, j_\phi = (1/r)\, d(r\, B_\theta)/dr$. The so-called "safety-factor", $q(r) = r\, B_\phi/(R_0\, B_\theta)$, parameterizes the helical pitches of equilibrium magnetic field-lines.

C. Plasma Response to RMP

Consider the response of the plasma to an externally generated, static, helical, RMP. Suppose that the RMP has m periods in the poloidal direction, and n periods in the toroidal direction. It is convenient to express the perturbed magnetic field and the perturbed plasma current density in terms of a perturbed poloidal magnetic flux (divided by $2\pi\, R_0$), $\psi(r,\theta,\phi,t)$. In fact, $\delta\mathbf{B} = \nabla\psi\times\nabla z$, and $\mu_0\,\delta\mathbf{j} = -\nabla^2\psi\,\nabla z$, where $\psi(r,\theta,\phi,t) = \hat{\psi}(r,t)\,\exp[\mathrm{i}\,(m\,\theta - n\,\phi)]$, and $\hat{\psi}$ is real. This particular representation is valid provided that $m/n \gg a/R_0$.[15]

The response of the plasma to the RMP is governed by the equations of marginally-stable, ideal-MHD everywhere in the plasma, apart from a relatively narrow (in r) region in the vicinity of the so-called "rational surface", minor radius r_s, at which $q(r_s) = m/n$.[15]

It is convenient to parameterize the RMP in terms of the so-called "vacuum magnetic flux", $\Psi_v(t) = |\Psi_v|\,\mathrm{e}^{-\mathrm{i}\,\varphi_v}$, which is defined to be the value of $\hat{\psi}(r,t)$ at radius r_s in the presence of the RMP, but in the absence of plasma. Here, φ_v is the helical phase of the RMP. Likewise, the response of the plasma in the vicinity of the rational surface is parameterized in terms of the so-called "reconnected magnetic flux", $\Psi_s(t) = |\Psi_s|\,\mathrm{e}^{\mathrm{i}\,\varphi_s}$, which is the actual value of $\hat{\psi}(r,t)$ at radius r_s. Here, φ_s is the helical phase of the reconnected magnetic flux.

The intrinsic stability of the m, n tearing mode is governed by the dimensionless parameter $E_{ss} = [d\hat{\psi}_s/d\ln r]_{r_s-}^{r_s+}$, where $\hat{\psi}_s(r)$ is a solution of the marginally-stable, ideal-MHD equations, for the case of an m, n helical perturbation, that satisfies physical boundary conditions at $r=0$ and $r=a$, in the absence of the RMP, and is such that $\hat{\psi}_s(r_s) = 1$.[10,16] According to resistive-MHD theory,[10,12] if $E_{ss} > 0$ then the m, n tearing mode spontaneously reconnects magnetic flux at the rational surface to form a helical magnetic island chain. In this paper, it is assumed that $E_{ss} < 0$, so that the m, n tearing mode is intrinsically stable. In this case, any magnetic reconnection that takes place at the rational surface is due solely to the action of the RMP.

The ideal-MHD response of the plasma to the RMP is governed by the dimensionless parameter $E_{sv} = [d\hat{\psi}_v/d\ln r]_{r_s-}^{r_s+}$, where $\hat{\psi}_v(r)$ is a solution of the marginally-stable, ideal-MHD equations, for the case of an m, n helical perturbation, that satisfies physical boundary conditions at $r=0$ and $r=a$, in the presence of the RMP, and is such that $\hat{\psi}_v(r_s) = 0$.[16]

D. Linear Response Regime

In the linear response regime, the reconnected magnetic flux induced by the RMP at the rational surface is governed by [15,26,27]

$$\frac{\delta_s}{r_s}\,\tau_R\left(\frac{d}{dt}+\mathrm{i}\,\omega_s\right)\Psi_s = E_{ss}\,\Psi_s + E_{sv}\,\Psi_v, \tag{1}$$

where δ_s is the linear layer width, $\tau_R = \mu_0\, r_s^2\,\sigma(r_s)$ the global resistive diffusion timescale, and

$$\omega_s(t) = m\,\Omega_\theta(r_s,t) - n\,\Omega_\phi(r_s,t). \tag{2}$$

Here, $\sigma(r)$, $\Omega_\theta(r,t)$, and $\Omega_\phi(r,t)$ are the plasma electrical conductivity, poloidal angular velocity, and toroidal angular velocity profiles, respectively. Note that, in this paper, we are assuming that the constant-ψ approximation [10] holds at the rational surface. (It is demonstrated in Ref. 28 that the appropriate linear response regime for an RMP resonant in the pedestal of a typical DIII-D H-mode discharge is the so-called "first semi-collisional regime", which is indeed a constant-ψ response regime. Moreover, if the appropriate linear response regime is constant-ψ then so is the appropriate nonlinear response regime, because the constant-ψ constraint is easier to satisfy in the nonlinear regime than in the linear regime.[26,29])

Equation (1) can be rewritten as an "amplitude evolution equation",

$$\frac{\delta_s}{r_s}\,\tau_R\,\frac{d|\Psi_s|}{dt} = E_{ss}\,|\Psi_s| + E_{sv}\,|\Psi_v|\,\cos(\varphi_s-\varphi_v), \tag{3}$$

combined with a "phase evolution equation",

$$\frac{d\varphi_s}{dt} = \omega_s - \frac{E_{sv}}{\tau_R}\,\frac{r_s}{\delta_s}\,\frac{|\Psi_v|}{|\Psi_s|}\,\sin(\varphi_s-\varphi_v). \tag{4}$$

The final term on the right-hand side of Eq. (4) is termed the "slip-frequency", and is the difference between the helical phase velocity of the reconnected magnetic flux and that expected on the assumption that the flux is convected by the plasma flow at the rational surface (i.e., $d\varphi_s/dt = \omega_s$). In general, the slip-frequency is non-zero because the plasma in the vicinity of the rational surface is capable of diffusing resistively through the linear layer structure.

E. Nonlinear Response Regime

In the nonlinear response regime, Eq. (3) generalizes to the "Rutherford island width evolution equation": [12,21]

$$\frac{(\mathcal{I}/2)\,W_s}{r_s}\,\tau_R\,\frac{d|\Psi_s|}{dt} = E_{ss}\,|\Psi_s| + E_{sv}\,|\Psi_v|\,\cos(\varphi_s-\varphi_v), \tag{5}$$

where

$$W_s = 4\left(\frac{|\Psi_s|}{s_s\,r_s\,B_\theta(r_s)}\right)^{1/2} r_s \tag{6}$$

is the full radial width of the magnetic island chain, $\mathcal{I} = 0.8227$, $s(r) = d\ln q/d\ln r$, and $s_s = s(r_s)$. The nonlinear regime holds when $W_s \gg \delta_s$, whereas the linear regime holds when $\delta_s \ll W_s$.

Equation (5) is usually coupled with the so-called "no-slip constraint": [15]

$$\frac{d\varphi_s}{dt} = \omega_s. \tag{7}$$

The reasoning behind the imposition of this constraint is that plasma is trapped inside the magnetic separatrix of the island chain that forms in the vicinity of the rational surface, which forces the chain to co-rotate with the local plasma flow. However, in reality, the plasma is able to diffuse resistively across the separatrix to some extent. Hence, by analogy with Eqs. (3), (4), and (5), and in accordance with Refs. 22 and 23, in this paper we shall modify Eq. (7) such that

$$\frac{d\varphi_s}{dt} = \omega_s - \frac{E_{sv}}{\tau_R}\,\frac{r_s}{(\mathcal{I}/2)\,W_s}\,\frac{|\Psi_v|}{|\Psi_s|}\,\sin(\varphi_s-\varphi_v). \tag{8}$$

The final term on the right-hand side of the previous equation is the "nonlinear slip-frequency". In general, we would expect this frequency to be relatively small (because it is usually the case that $|\omega_s|\,\tau_R\,(W_s/r_s) \gg 1$ for fully-developed magnetic islands in high-temperature tokamak plasmas [23,28]). Nevertheless, the nonlinear slip-frequency may be non-negligible for developing island chains, which is why we are including it in our analysis. (Note that the nonlinear slip-frequency does not appear in rigorous island calculations, such as that described in Ref. 30, and references therein, because such calculations depend crucially on complicated hierarchical ordering assumptions, according to which the nonlinear slip-frequency is negligible.)

F. Composite Model

We can combine Eqs. (3), (4), (5), and (8) to give the following composite resonant response model that interpolates between the linear and the nonlinear regimes:

$$\left(\frac{(\mathcal{I}/2)\,W_s+\delta_s}{r_s}\right)\tau_R\,\frac{d|\Psi_s|}{dt}=E_{ss}\,|\Psi_s|+E_{sv}\,|\Psi_v|\,\cos(\varphi_s-\varphi_v),\tag{9}$$

$$\frac{d\varphi_s}{dt}=\omega_s-\frac{E_{sv}}{\tau_R}\left(\frac{r_s}{(\mathcal{I}/2)\,W_s+\delta_s}\right)\frac{|\Psi_v|}{|\Psi_s|}\,\sin(\varphi_s-\varphi_v).\tag{10}$$

If we define $X_s=|\Psi_s|\,\cos\varphi_s$, $Y_s=|\Psi_s|\,\sin\varphi_s$, $X_v=|\Psi_v|\,\cos\varphi_v$, and $Y_v=|\Psi_v|\,\sin\varphi_v$ then the previous two equations are more conveniently written in the non-singular (when $|\Psi_s|=0$) forms: [22,23,31]

$$\left(\frac{(\mathcal{I}/2)\,W_s+\delta_s}{r_s}\right)\tau_R\left(\frac{dX_s}{dt}+\omega_s\,Y_s\right)=E_{ss}\,X_s+E_{sv}\,X_v,\tag{11}$$

$$\left(\frac{(\mathcal{I}/2)\,W_s+\delta_s}{r_s}\right)\tau_R\left(\frac{dY_s}{dt}-\omega_s\,X_s\right)=E_{ss}\,Y_s+E_{sv}\,Y_v,\tag{12}$$

where

$$W_s=4\left(\frac{\sqrt{X_s^{\,2}+Y_s^{\,2}}}{s_s\,r_s\,B_\theta(r_s)}\right)^{1/2}r_s.\tag{13}$$

With the benefit of hindsight, Eqs. (11) and (12) could have been derived more directly from the following heuristic generalization of Eq. (1): [23]

$$\left(\frac{(\mathcal{I}/2)\,W_s+\delta_s}{r_s}\right)\tau_R\left(\frac{d}{dt}+\mathrm{i}\,\omega_s\right)\Psi_s=E_{ss}\,\Psi_s+E_{sv}\,\Psi_v.\tag{14}$$

III. MODIFIED TOROIDAL RESONANT RESPONSE MODEL

Let us now generalize our investigation to toroidal geometry.

The toroidal model of the response of a tokamak plasma to a static, externally generated, RMP that is implemented in the `EPEC` code [25] is described in detail in Ref. 24. In the light of the composite cylindrical resonant response model developed in Sect. II, we propose to modify the resonant response component of the `EPEC` model (this component is described in Appendix D of Ref. 24).

Equations (D1) and (D2) in Ref. 24 are modified such that

$$\left(\hat{W}_k + \hat{\delta}_k\right) \mathcal{S}_k \frac{d\hat{\Psi}_k}{d\hat{t}} = \sum_{k'=1,K} \hat{E}_{kk'}\, \hat{\Psi}_{k'}\, \cos(\varphi_k - \varphi_{k'} - \xi_{kk'}) + \hat{E}_{kk}\, \hat{\chi}_k\, \cos(\varphi_k - \zeta_k), \tag{15}$$

$$\mathcal{S}_k = \frac{\tau_R(\hat{r}_k)}{\tau_A}, \tag{16}$$

respectively. Here,

$$\hat{W}_k = \frac{2\,\mathcal{I}}{\hat{a}\,\hat{r}_k} \left(\frac{q}{g\,s}\right)^{1/2}_{\hat{r}_k} |\hat{\Psi}_k|^{\,1/2}, \tag{17}$$

$$\hat{\delta}_k = \frac{\delta_{\rm SC}(\hat{r}_k)}{R_0\,\hat{a}\,\hat{r}_k}, \tag{18}$$

where $\delta_{\rm SC}(\hat{r})$ is the semi-collisional linear layer width specified in Ref. 28.

In the previous expressions, R_0 is the major radius of the magnetic axis, r is a magnetic flux-surface label with dimensions of length (which, roughly speaking, is the average minor radius of the flux-surface), $q(r)$ is the safety-factor profile, $s(r) = d\ln q/d\ln r$, $g(r)\,B_0$ is the toroidal magnetic field-strength at major radius R_0, B_0 is the vacuum toroidal magnetic field-strength on the magnetic axis, a is the value of r on the last closed magnetic flux-surface, r_k is the value of r on the kth rational surface (resonant with poloidal mode number m_k, and toroidal mode number n), $\hat{a} = a/R_0$, $\hat{r} = r/a$, and $\hat{r}_k = r_k/a$. Furthermore, $\tau_R(\hat{r}) = \mu_0\, r^{\,2}\, \sigma_{ee}\, Q^{ee}_{00}$, where σ_{ee} is the classical plasma parallel electrical conductivity, and Q^{ee}_{00} describes the corrections to this conductivity due to neoclassical effects and the presence of plasma impurities. Also, τ_A is a convenient scale time, and $\hat{t} = t/\tau_A$. Finally, $\Psi_k = B_0\, R_0\, \hat{\Psi}_k\, {\rm e}^{-{\rm i}\,\varphi_k}$ is the reconnected magnetic flux at the kth rational surface, $\chi_k = B_0\, R_0\, \hat{\chi}_k\, {\rm e}^{-{\rm i}\,\zeta_k}$ is a measure of the vacuum magnetic flux at the kth rational surface (in fact, $\hat{E}_{kk}\,\chi_k$ is equivalent to $E_{sv}\,\Psi_v$ in Sect. II), and $E_{kk'} = \hat{E}_{kk'}\, {\rm e}^{-{\rm i}\,\xi_{kk'}}$ is the toroidal tearing stability matrix.[16] Here, $\hat{\Psi}_k > 0$, φ_k, $\hat{\chi}_k > 0$, ζ_k, $\hat{E}_{kk'} > 0$, and $\xi_{kk'}$ are all real quantities.

Equation (15) represents a minor improvement to Eq. (D1) of Ref. 24 in which the interpolation between the linear and nonlinear regimes is performed in a slightly more accurate manner.

Equation (D6) of Ref. 24 is modified such that

$$\left(\hat{W}_k + \hat{\delta}_k\right) \mathcal{S}_k \left(\frac{d\varphi_k}{d\hat{t}} - \hat{\varpi}_k\right) = -\sum_{k'=1,K} \hat{E}_{kk'}\, \hat{\Psi}_{k'}\, \sin(\varphi_k - \varphi_{k'} - \xi_{kk'}) - \hat{E}_{kk}\, \hat{\chi}_k\, \sin(\varphi_k - \zeta_k), \tag{19}$$

where

$$\hat{\varpi}_k = \hat{\varpi}_{k\,0} + m_k\,\Delta\hat{\Omega}_\theta(\hat{r}_k,\hat{t}) - n\,\Delta\hat{\Omega}_\phi(\hat{r}_k,\hat{t}), \tag{20}$$

and $\hat{\varpi}_{k\,0} = \varpi_{k\,0}\,\tau_A$, $\hat{\Omega}_\theta = \Delta\Omega_\theta\,\tau_A$, and $\hat{\Omega}_\phi = \Delta\Omega_\phi\,\tau_A$. Here, $\varpi_{k\,0}$ is the so-called "natural frequency" (in the absence of the RMP) at the kth rational surface; this quantity is defined as the helical phase velocity of a naturally unstable island chain, resonant at the surface, in the absence of an RMP (or any other island chains). On the other hand, $\Delta\Omega_\theta$ and $\Delta\Omega_\phi$ are the changes in the plasma poloidal and toroidal velocity profiles, respectively, induced by the electromagnetic torques that develop in the vicinities of the various rational surfaces in the plasma in response to the RMP. Equation (19) represents a major improvement to Eq. (D6) of Ref. 24 that takes into account the finite slip-frequencies of the magnetic island chains induced at the various rational surfaces in the plasma. In the absence of a finite slip-frequency, the right-hand side of Eq. (19) would be zero.

If we define $X_k = \hat{\Psi}_k\,\cos\varphi_k$ and $Y_k = \hat{\Psi}_k\,\sin\varphi_k$ then Eqs. (15) and (19) are more conveniently written in the non-singular (when $\hat{\Psi}_k = 0$) forms

$$\left(\hat{W}_k + \hat{\delta}_k\right)\mathcal{S}_k\left(\frac{dX_k}{d\hat{t}} + \hat{\varpi}_k\,Y_k\right) = \sum_{k'=1,K}\hat{E}_{kk'}\,(\cos\xi_{kk'}\,X_{k'} - \sin\xi_{kk'}\,Y_{k'}) + \hat{E}_{kk}\,\hat{\chi}_k\,\cos\zeta_k, \tag{21}$$

$$\left(\hat{W}_k + \hat{\delta}_k\right)\mathcal{S}_k\left(\frac{dY_k}{d\hat{t}} - \hat{\varpi}_k\,X_k\right) = \sum_{k'=1,K}\hat{E}_{kk'}\,(\cos\xi_{kk'}\,Y_{k'} + \sin\xi_{kk'}\,X_{k'}) + \hat{E}_{kk}\,\hat{\chi}_k\,\sin\zeta_k, \tag{22}$$

where

$$\hat{W}_k = \frac{2\,\mathcal{I}}{\hat{a}\,\hat{r}_k}\left(\frac{q}{g\,s}\right)^{1/2}_{\hat{r}_k}(X_k^2 + Y_k^2)^{\,1/4}. \tag{23}$$

Equations (15), (19), (21), (22) and (23) are the toroidal generalizations of Eqs. (9), (10), (11), (12), and (13), respectively.

IV. EPEC MODELING OF DIII-D DISCHARGE #145380

A. Introduction

DIII-D discharge #145380 is an ITER-Similar-Shape (ISS), ELMing, H-mode discharge, with a toroidal magnetic field $B_T = -1.9\,\mathrm{T}$, in which the plasma current, I_p, is slowly ramped

over a 2 second interval in order to scan the magnetic safety-factor.[32,33] The majority ions are Deuterium, whereas the minority ions are Carbon VI. Figure 1 gives an overview of this discharge. Ψ_N is the conventional normalized poloidal magnetic flux. A static RMP is applied to the plasma by running steady $n = 3$ currents through the I-coil system.[34] Three windows of ELM suppression or mitigation are evident: the first (in which ELMs are mitigated, but not entirely suppressed) extends from $t = 2840$–2980 ms; the second (in which ELM are entirely suppressed) extends from $t = 3320$–3560 ms; and the third (in which ELMs are entirely suppressed) extends from $t = 3880$–4200 ms. The first, second, and third ELM-suppression/mitigation windows extend over the $\overline{q_{95}}$ ranges 3.88–3.94, 3.62–3.73, and 3.33–3.48, respectively. Here, $\overline{q_{95}}$ is least-squares linear fit to the variation of the safety-factor at the $\Psi_N = 0.95$ flux-surface with time.

B. Relaxation of No-Slip Constraint

As is discussed in Ref. 25, the best agreement between the predictions of the `EPEC` code and experimental observations is obtained by assuming that the unperturbed natural frequencies at the various rational surfaces in the plasma are determined by the local equilibrium $\mathbf{E}\times\mathbf{B}$ frequencies. In other words,

$$\varpi_{k\,0} = -n\,\omega_E(\Psi_{p\,k}), \tag{24}$$

where

$$\omega_E(\Psi_p) = -\frac{d\Phi}{d\Psi_p}. \tag{25}$$

Here, $\Phi(\Psi_p)$ is the equilibrium scalar electric potential (in the absence of the RMP), Ψ_p the equilibrium poloidal magnetic flux (divided by 2π), and $\Psi_{p\,k}$ the value of Ψ_p at the kth rational surface. Equation (24) holds at every rational surface in all of the simulations discussed in Sect. IV B.

1. No-Slip Constraint Imposed

In our first simulation, the no-slip constraint is imposed at all rational surfaces in the plasma. This implies that the resonant response model at the kth rational surface consists of Eq. (15) and Eq. (19), with the right-hand side of the latter equation set to zero; in other words, the slip-frequency is set to zero at the kth rational surface.

The upper panel of Fig. 2 shows the natural frequencies, in the absence of the RMP, of the various $n = 3$ tearing modes that are resonant in the pedestal of DIII-D discharge #145380. It can be seen that the natural frequencies of the $m = 11$ (brown), the $m = 10$ (magenta), and the $m = 9$ (cyan), tearing modes have their zero-crossings in the first, second, and third, ELM-suppression/mitigation window, respectively. The lower panel of Fig. 2 shows the natural frequencies, in the presence of the RMP, of the various $n = 3$ tearing modes that are resonant in the pedestal. It is apparent that if the magnitude of the natural frequency in the absence of the RMP falls below about 3 krad/s then the associated tearing mode locks to the RMP (i.e., its true natural frequency becomes zero).

The upper panel of Fig. 3 shows the widths of the various vacuum magnetic island chains driven by the applied $n = 3$ RMP in the pedestal region as functions of $\overline{q_{95}}$. The vacuum island widths are the expected island widths in the absence of any shielding of driven magnetic reconnection due to plasma flow; in other words, they are the widths of the island chains that would be driven if all of the natural frequencies were zero. It can be seen that the driven magnetic island chains extend over most of the pedestal, implying a very significant degradation in pedestal energy and particle confinement due to the expected flattening of the density and temperature profiles across the chains.[36] Moreover, the driven island chains at the bottom of the pedestal overlap, implying that the magnetic field in this region is rendered stochastic. The lower panel of Fig. 3 shows the predicted widths of the various magnetic island chains driven by the applied $n = 3$ RMP as functions of time. It is apparent that the predicted island widths are generally much smaller than the vacuum island widths, as a consequence of the shielding of driven magnetic reconnection due to plasma flow. However, the shielding breaks down at various rational surfaces when the associated natural frequency is zero (see the lower panel of Fig. 3). In this situation, the driven island width is similar to the vacuum island width.

According to the prevailing hypothesis, RMP-induced ELM mitigation/suppression in an H-mode tokamak discharge occurs when a comparatively wide, locked, magnetic island chain is generated at the top of the pedestal.[35] The temperature and density flattening associated with the chain is presumed to limit the radial expansion of the pedestal, and, thereby, prevent it from attaining a width sufficient to destabilize peeling-ballooning modes[37] (which are thought to trigger ELMs).[32] It has also been suggested that the well-known "density pump-out" phenomenon, which is often observed when RMPs are applied to H-mode tokamak

plasmas, is associated with the formation of overlapping island chains at the bottom of the pedestal.[35]

According to Fig. 3, the comparatively wide, $m = 11$ (brown), $m = 10$ (magenta), and $m = 9$ (cyan), locked magnetic island chains which are predicted to be driven by the RMP in the pedestal of DIII-D discharge #145380 line up fairly well with the first, second, and third, ELM-suppression/mitigation windows, respectively. To be more exact, the island chains are located at the top of the pedestal (i.e., $\Psi_N = 0.925$), and also occur in roughly the correct time intervals. This is consistent with the hypothesis that the formation of locked magnetic island chains at the top of the pedestal causes ELM mitigation/suppression. Note that overlapping island chains are also driven at the bottom of the pedestal; as has already been mentioned, such island chains are associated with the density pump-out phenomenon.

In principle, the calculation shown in Figs. 2 and 3 is a repeat of one performed in Ref. 25. In practice, there is a slight difference between the two calculations because the expression for the linear layer width used in Eq. (D1) of Ref. 24 (which specifies the island width evolution equation employed in Ref. 25), which was only intended to be approximate, is slightly inaccurate [because it contains a spurious factor of $(2\,\mathcal{I}/\hat{a})\,(q/g\,s)^{1/2}_{\hat{r}_k}$]. This accounts for the very minor differences between Figs. 2 and 3 in this paper, and Figs. 8 and 9 in Ref. 25.

2. No-Slip Constraint Relaxed

In our second simulation, the no-slip constraint is relaxed at all rational surfaces in the plasma. This implies that the resonant response model at the kth rational surface consists of Eqs. (21) and (22). Figures 4 and 5 show analogous data to Figs. 2 and 3, respectively. Figure 6 shows details of the bottom panels of Figs. 2 and 4, in order to better illustrate the island chain dynamics when the RMP-modified natural frequencies of the various $n = 3$ tearing modes in plasma are comparatively small.

A comparison of Figs. 2 and 4, as well as an examination of Fig. 6, reveals that the relaxation of the no-slip constraint facilitates the locking of magnetic island chains to the RMP to a relatively modest degree. (Here, by locking, we mean a reduction in the RMP-modified natural frequency to a value close to zero.) This is not surprising, since relaxation of the no-slip constraint clearly weakens the coupling between a given magnetic island chain

and the local plasma flow (which is ultimately responsible for the shielding of driven magnetic reconnection). It can be seen from Fig. 6 that if the no-slip constraint is imposed then the RMP-modified natural frequencies of locked magnetic island chains are exactly zero. On the other hand, if the no-slip constraint is relaxed then locked magnetic island chains possess small but finite RMP-modified natural frequencies, because the local plasma flow is able to slip through the stationary chains to some extent. However, the degree of slippage for a fully developed locked magnetic island chain is comparatively small (i.e., no more than 0.5 krad/s), which helps explain why the no-slip constraint can be used to accurately predict the dynamics of wide magnetic island chains in tokamaks and reversed field pinches.[38]

It is remarkable that the results shown in Figs. 2–4 are so similar, given that the relaxation of the no-slip constraint leads to a radical modification of the dynamics of non-locked magnetic island chains. When the no-slip constraint is imposed, the widths of magnetic island chains that are unable to lock to the RMP are forced to pulsate, periodically falling to zero, because the helical phases of the chains are forced to continuously increase (or decrease) by their non-zero natural frequencies.[26–28,30,39] On the other hand, when the no-slip constraint is relaxed, the widths of magnetic island chains that are unable to lock to the RMP have steady values, because the chains can slip with respect to the local plasma flow, which means that they can have fixed helical phases despite the fact that their natural frequencies are non-zero.

C. Improved Interpolation between Linear and Nonlinear Resonant Response Regimes

According to linear tearing mode theory, in the absence of the RMP, the natural frequency of the tearing mode resonant at the kth rational surface is given by [13,40–42]

$$\varpi_{k\,0} = \varpi_{\ln k} \equiv -n\,(\omega_E + \omega_{*\,e})_{\Psi_{p\,k}}, \tag{26}$$

where

$$\omega_{*\,e}(\Psi_p) = \frac{T_e}{e}\,\frac{d\ln p_e}{d\Psi_p}. \tag{27}$$

Here, e is the magnitude of the electron charge, $p_e(\Psi_p)$ the equilibrium (i.e., in the absence of the RMP) electron pressure, and $T_e(\Psi_p)$ the equilibrium electron temperature.

According to nonlinear tearing mode theory, in the absence of the RMP, the natural frequency of the tearing mode resonant at the kth rational surface is given by [24]

$$\varpi_{k\,0} = \varpi_{\rm nl\,k} \equiv -n \left(\omega_E + \left[1 - L_{00}^{ii} + L_{01}^{ii} \left(\frac{\eta_i}{1+\eta_i} \right) \right] \omega_{*\,i} - \left[L_{00}^{iI} - L_{01}^{iI} \left(\frac{\eta_I}{1+\eta_I} \right) \right] \omega_{*\,I} \right)_{\Psi_{p\,k}}, \tag{28}$$

where

$$\omega_{*\,a}(\Psi_p) = -\frac{T_a}{Z_a\,e}\,\frac{d\ln p_a}{d\Psi_p}, \tag{29}$$

$$\eta_a(\Psi_p) = \frac{d\ln T_a}{d\ln n_a}, \tag{30}$$

for $a = i, I$. Here, Z_i, $n_i(\Psi_p)$, $T_i(\Psi_p)$, and $p_i(\Psi_p) = n_i\,T_i$ are the charge number, equilibrium number density, equilibrium temperature, and equilibrium pressure of the majority (thermal) ions, respectively, whereas Z_I, n_I, T_I, $p_I = n_I\,T_I$ are the corresponding quantities for the impurity ions. Furthermore, $L_{00}^{ii}(\Psi_p)$, $L_{01}^{ii}(\Psi_p)$, $L_{00}^{II}(\Psi_p)$, and $L_{01}^{II}(\Psi_p)$ are neoclassical parameters that are defined in Sect. B of Ref. 24.

Finally, the best agreement between theory and experiment is obtained by assuming that, in the absence of the RMP, the natural frequency of the tearing mode resonant at the kth rational surface is given by [25,43]

$$\varpi_{k\,0} = \varpi_{\rm eb\,k} \equiv -n\,(\omega_E)_{\Psi_{p\,k}}. \tag{31}$$

1. Linear Calculation

For the sake of comparison, we shall first perform a purely linear calculation. Thus, the resonant plasma response model at the kth rational surface consists of Eqs. (21) and (22), with $\hat{W}_k$ set to zero. Moreover, in the absence of the RMP, the natural frequency at the kth rational surface is specified by Eq. (26). Figures 7 and 8 show the natural frequencies in the absence, and in the presence, of the RMP, as well as the vacuum islands widths and the actual island widths.

2. Composite Linear/Nonlinear Calculation

In our composite linear/nonlinear calculation, the resonant plasma response model at the kth rational surface consists of Eqs. (21) and (22). Moreover, in the absence of the RMP,

the natural frequency at the kth rational surface is specified by

$$\varpi_{k\,0} = \frac{\varpi_{\ln k} + (\varpi_{\rm eb\,k} - \varpi_{\ln k} - \varpi_{\rm nl\,k})\, x_k + \varpi_{\rm nl\,k}\, x_k^2}{1 - x_k + x_k^2}, \tag{32}$$

where $x_k = \hat{W}_k/\hat{\delta}_k$. It follows that $\varpi_{k\,0} = \varpi_{\ln k}$ in the linear regime, $x_k \ll 1$; $\varpi_{k\,0} = \varpi_{\rm nl\,k}$ in the nonlinear regime, $x_k \gg 1$; and $\varpi_{k\,0} = \varpi_{\rm eb\,k}$ when $x_k = 1$. (Note that $\varpi_{\rm eb\,k}$ generally lies between $\varpi_{\ln k}$ and $\varpi_{\rm nl\,k}$.) Figures 9 and 10 show the natural frequencies in the absence, and in the presence, of the RMP, as well as the vacuum islands widths and the actual island widths.

It can be seen, by a comparison of Figs. 7–10, that the linear calculation very significantly overestimates how easy it is for magnetic island chains to lock to the RMP. The reason for this is that the linear slip-frequency is comparatively high, because the linear layer width is comparatively narrow. The true slip-frequency becomes less than the linear slip-frequency as soon as the island width exceeds the linear layer width. [See Eq. (10).] The fact that the linear calculation is highly inaccurate confirms the conclusion reached in Ref. 28 that the response of a typical H-mode tokamak plasma to an RMP is not governed by linear theory, because the driven island widths exceed the very narrow linear layer widths, even when driven reconnection is strongly suppressed by plasma flow.

Intriguingly, the composite linear/nonlinear model fairly accurately predicts the temporal extends of the three ELM mitigation/suppression windows (assuming that the windows correspond to the formation of wide locked magnetic island chains at the top of the pedestal). However, the windows do not occur in the correct time intervals. We conclude that Eq. (31) gives a more accurate prediction for the natural frequencies, in the absence of the RMP, than Eq. (32). However, the reason for this is, as yet, unclear.

V. SUMMARY

We have developed an improved resonant plasma response model that describes the interaction between a tokamak plasma and an RMP. The model interpolates between the linear and the nonlinear response regimes, and takes into account the fact that the slip-frequency is non-zero in the nonlinear regime. Our improved model has been incorporated into the `EPEC` toroidal asymptotic matching code.[25] The modified `EPEC` code is used to model RMP-induced ELM mitigation/suppression in DIII-D H-mode discharge #145380.

We find that allowing for a finite slip-frequency (i.e., relaxing the so-called no-slip constraint) slightly facilitates the locking of driven magnetic island chains to the RMP. (Here, by locking, we mean the reduction of the true natural frequency of a given chain to a value that is very close to zero.) In fact, there is surprisingly little difference between `EPEC` simulations that impose the no-slip constraint at the various rational surfaces in the plasma and those in which the constraint is relaxed. This is true despite the fact that the nature of non-locked island solutions is radically different in the two cases (in the first case, the widths of the island chains driven at the rational surfaces pulsate, in the second they remain steady).

Our calculations confirm the conclusion reached in Ref. 28 that the response of a typical H-mode tokamak plasma to an RMP cannot be accurately modeled by linear theory. Our calculations also confirm the conclusion reached in Ref. 25 that the best agreement between theory and observations is obtained by assuming that the natural frequencies of tearing modes, in the absence of the RMP, are determined by the local $\mathbf{E} \times \mathbf{B}$ frequency.

ACKNOWLEDGEMENTS

This research was directly funded by the U.S. Department of Energy, Office of Science, Office of Fusion Energy Sciences, under contract DE-FG02-04ER54742, and incorporates work funded by the U.S. Department of Energy, Office of Science, Office of Fusion Energy Sciences, using the DIII-D National Fusion Facility, a DOE Office of Science user facility, under contract DE-FC02-04ER54698.

DISCLAIMER

DATA AVAILABITY STATEMENT

The data that support the findings of this study are available from the corresponding author upon reasonable request.

REFERENCES

[1] J.T. Scoville, and R.J. La Haye, Nucl. Fusion **43**, 250 (2003).

[2] J.-K. Park, M.J. Schaffer, J.E. Menard, and A.H. Boozer Phys. Rev. Lett. **99**, 195003 (2007).

[3] N.M. Ferraro, J.-K. Park, C.E. Myers, A. Brooks, S.P. Gerhardt, J.E. Menard, S. Munaretto, and M.L. Reinke, Nucl. Fusion **59**, 086021 (2019).

[4] T.E. Evans, R.A. Moyer, J.G. Watkins, P.R. Thomas, T.H. Osborne, J.A. Boedo, M.E. Fenstermacher, K.H. Finken, R.J. Groebner, M. Groth, *et al.*, Phys. Rev. Lett. **92**, 235003 (2004).

[5] Y. Liang, H.R. Koslowski, P.R. Thomas, E. Nardon, B. Alper, P. Andrew, Y. Andrew, G. Arnoux, Y. Baranov, M. Bécoulet, *et al.*, Phys. Rev. Lett. **98**, 265004 (2007).

[6] W. Suttrop, T. Eich, J.C. Fuchs, S. Günter, A. Janzer, A. Herrmann, A. Kallenbach, P.T. Lang, T. Lunt, M. Maraschek, *et al.*, Phys. Rev. Lett. **106**, 225004 (2011).

[7] Y.M. Jeon, J.-K. Park, S.W. Yoon, W.H. Ko, S.G. Lee, K.D. Lee, G.S. Yun, Y.U. Nam, W.C. Kim, J.-G. Kwak, K.S. Lee, H.K. Kim, and H.L. Yang, *et al.*, Phys. Rev. Lett. **109**, 035004 (2012).

[8] A. Kirk, I.T. Chapman, Y. Liu, P. Cahyna, P. Denner, G. Fishpool, C.J. Ham, J.R. Harrison, Y. Liang, E. Nardon, S. Saarelma, R. Scannell, A.J. Thornton, and MAST Team, Nucl. Fusion **53**, 043007 (2013).

[9] T. Sun, Y. Liang, Y.Q. Liu, S. Gu, X. Yang, W. Guo, T. Shi, M. Jia, L. Wang, B. Lyu, *et al.*, Phys. Rev. Lett. **117**, 115001 (2016).

[10] H.P. Furth, J. Killeen, and M.N. Rosenbluth, Phys. Fluids **6**, 459 (1963).

[11] B. Coppi, J.M. Greene, and J.L. Johnson, Nucl. Fusion **6**, 101 (1966).

[12] P.H. Rutherford, Phys. Fluids **16**, 1903 (1973).

[13] G. Ara, B. Basu, B. Coppi, G. Laval, M.N. Rosenbluth, and B.V. Waddell, Ann. Phys. (N.Y.) **112**, 443 (1978).

[14] A. Pletzer, and R.L. Dewar, J. Plasma Physics **45**, 427 (1991).

[15] R. Fitzpatrick, Nucl. Fusion **33**, 1049 (1993).

[16] R. Fitzpatrick, R.J. Hastie, T.J. Martin, and C.M. Roach, Nucl. Fusion **33**, 1533 (1993).

[17] S. Tokuda, Nucl. Fusion **41**, 1037 (2001).

[18] D.P. Brennan, R.J. La Haye, A.D. Turnbull, M.S. Chu, T.H. Jensen, L.L. Lao, T.C. Luce, P.A. Politzer, and E.J. Strait, Phys. Plasmas **10**, 1643 (2003).

[19] A.H. Glasser, Z.R. Wang, and J.-K. Park, Phys. Plasmas **23**, 112506 (2016).

[20] R. Fitzpatrick, Phys. Plasmas **24**, 072506 (2017).

[21] P.H. Rutherford, in *Basic Physical Processes of Toroidal Fusion Plasmas*, Proc. Course and Workshop, Varenna, 1985. (Commission of the European Communities, Brussels, 1985.) Vol. 2, p. 531.

[22] L.G. Eliseev, N.V. Ivanov, A.M. Kakurin, A.V. Melnikov, and S.V. Perfilov, Phys. Plasmas **22**, 052504 (2015).

[23] W. Huang, and P. Zhu, Phys. Plasmas **27**, 022514 (2020).

[24] R. Fitzpatrick, and A.O. Nelson, Phys. Plasmas **27**, 072501 (2020).

[25] R. Fitzpatrick, Phys. Plasmas **27**, 102511 (2020).

[26] R. Fitzpatrick, Phys. Plasmas **5**, 3325 (1998).

[27] R. Fitzpatrick, Phys. Plasmas **21**, 092513 (2014).

[28] R. Fitzpatrick, Phys. Plasmas **27**, 042506 (2020).

[29] R. Fitzpatrick, Phys. Plasmas **10**, 2304 (2003).

[30] R. Fitzpatrick, Phys. Plasmas **25**, 082513 (2018).

[31] A.N. Chudnovskiy, Y.V. Gvozdkov, N.V. Ivanov, A.M. Kakurin, A.A. Medvedev, I.I. Orlovskiy, Y.D. Pavlov, V.V. Piterskiy, V.D. Pustovitov, M.B. Safonova, V.V. Volkov, and the T-10 Team, Nucl. Fusion **43** 681 (2003).

[32] P.B. Snyder, T.H. Osboune, K.H. Burrell, R.J. Groebner, A.W. Leonard, R. Nazikian, D.M. Orlov, O. Schmitz, M.R. Wade, and H.R. Wilson, Phys. Plasmas **19**, 056115 (2012).

[33] Q.M. Hu, R. Nazikian, B.A. Grierson, N.C. Logan, D.M. Orlov, C. Paz-Solden, and Q. Yu, Phys. Rev. Lett. **125**, 045001 (2020).

[34] G.L. Jackson, P.M. Anderson, J. Bialek, W.P. Cary, G.L. Campbell, A.M. Garofalo, R. Hatcher, A.G. Kellman, R.J. La Haye, A. Nagy, *et al.*, Proc. 30th EPS Conf. on Controlled Fusion and Plasma Physics. (St. Petersburg, Russia, 2003) CD-ROM, P-4.47.

[35] Q.M. Hu, R. Nazikian, B.A. Grierson, N.C. Logan, J.-K. Park, C. Paz-Soldan, and Q. Yu, Phys. Rev. Lett. **125**, 045001 (2020).

[36] R. Fitzpatrick, Phys. Plasmas **2**, 825 (1995).

[37] J.W. Connor, R.J. Hastie, H.R. Wilson, and R.L. Miller, Phys. Plasmas **5**, 2687 (1998).

[38] B.E. Chapman, R. Fitzpatrick, D. Craig, P. Martin, and G. Spizzo, Phys. Plasmas **11**, 2156 (2004).

[39] R. Fitzpatrick, Phys. Plasmas **25**, 112505 (2018).

[40] M. Bécoulet, F. Orain, P. Maget, N. Mellet, X. Garbet, E. Nardon, G.T.A. Huysmans, T. Casper, A. Loarte, P. Cayna, *et al.*, Nucl. Fusion **52**, 054003 (2012).

[41] N.M. Ferraro, Phys. Plasmas **19**, 056105 (2012).

[42] F. Orain, M. Bécoulet, G. Dif-Pradalier, G.T.A. Huysmans, S. Pamela, E. Nardon, C. Passeron, G. Latu, V. Grandgirard, A. Fil, *et al.*, Phys. Plasmas **20**, 102510 (2013).

[43] M.F. Heyn, I.B. Ivanov, S.V. Kasilov, W. Kernbichler, I. Joseph, R.A. Moyer, and A.M. Runov, Nucl. Fusion **48**, 024005 (2008).

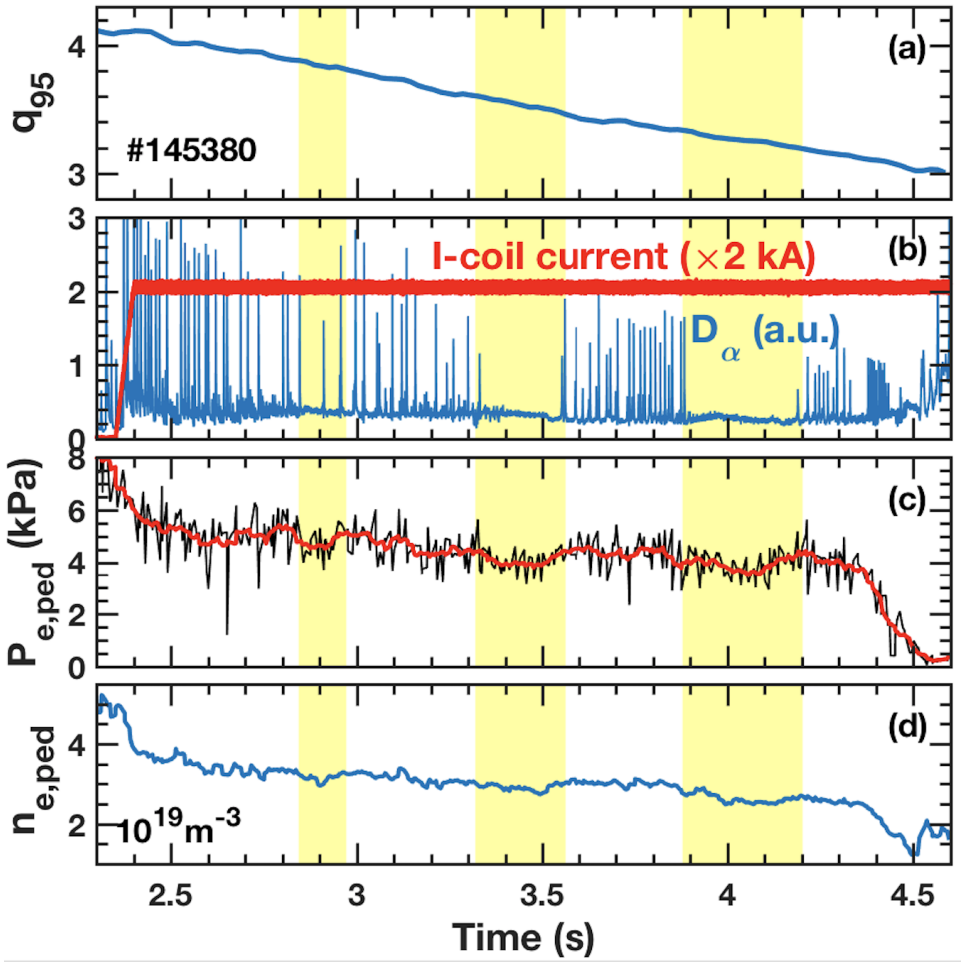

FIG. 1. Overview of DIII-D discharge #145380. (a) Safety factor at $\Psi_N = 0.95$. (b) D_α (i.e., Deuterium Balmer-alpha) signal, as well as $n = 3$ current flowing in upper and lower sections of I-coil. (c) Pedestal (i.e., $\Psi_N = 0.94$) electron pressure. (The red curve is the running average over 10 ms.) (d) Pedestal electron number density. The common vertical yellow bands indicate the ELM-suppression/mitigation windows.

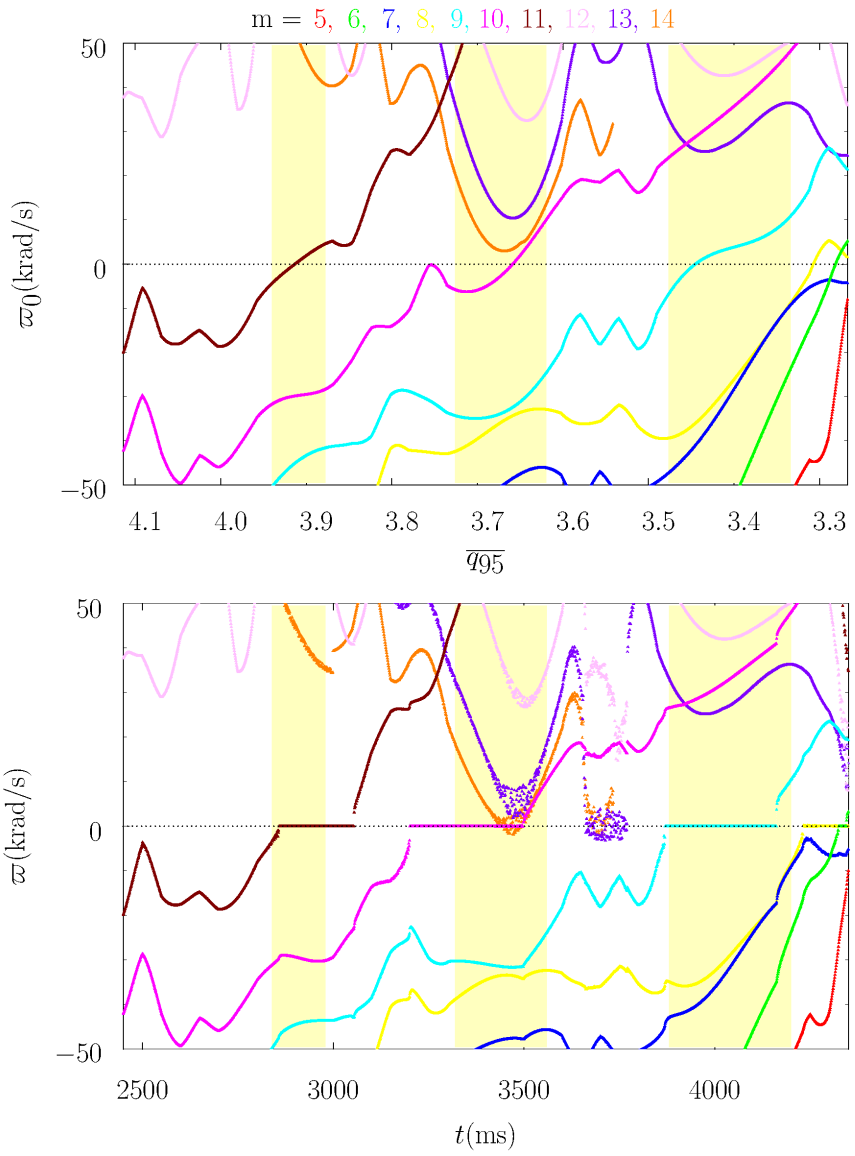

FIG. 2. Composite linear/nonlinear calculation with the no-slip constraint imposed at all rational surfaces, and the natural frequencies in the absence of the RMP determined by the local $\mathbf{E} \times \mathbf{B}$ frequency. Top Panel: $n = 3$ natural frequencies, in absence of RMP, as functions of the least-squares linear fit to q_{95} versus time in DIII-D discharge #145380. Bottom Panel: $n = 3$ natural frequencies, in presence of RMP, as functions of time in DIII-D discharge #145380. The red, green, blue, yellow, cyan, magenta, brown, pink, purple, and orange curves correspond to $m = 5$, 6, 7, 8, 9, 10, 11, 12, 13, and 14, respectively. The yellow vertical bands indicate the ELM-suppression windows.

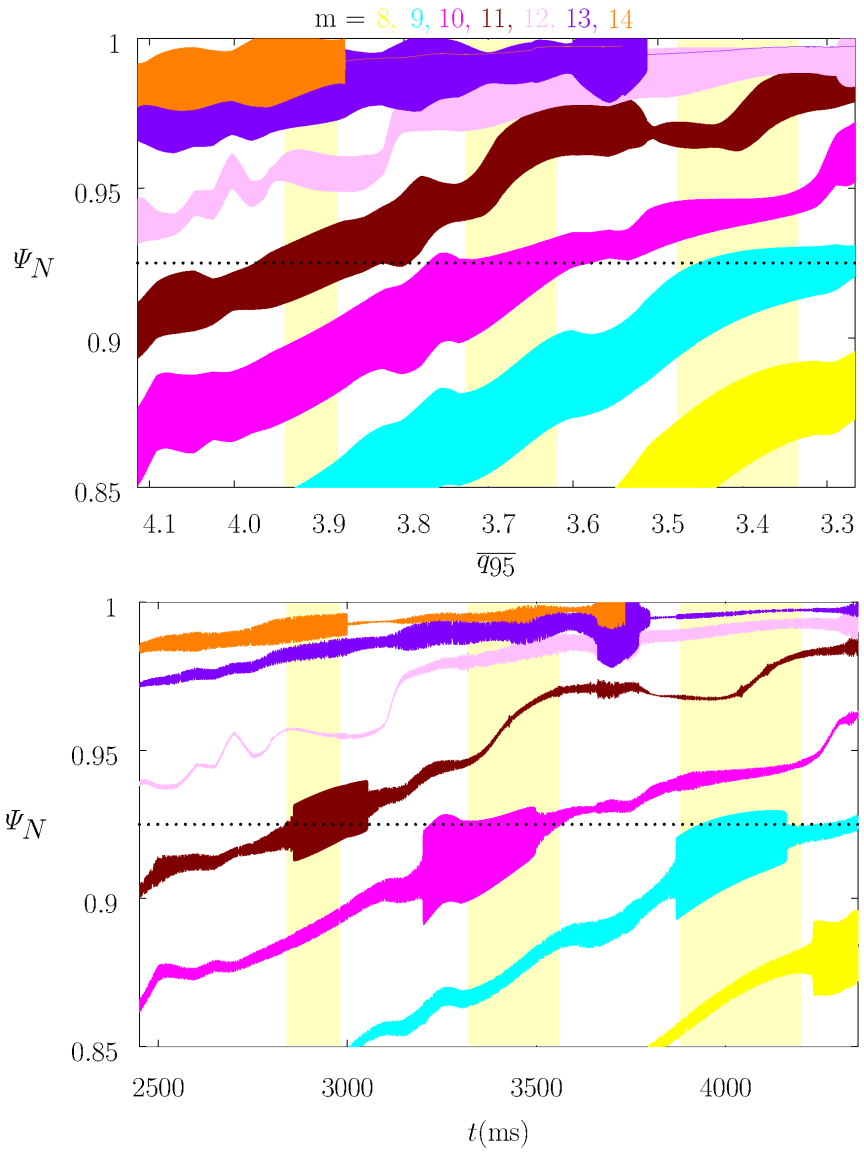

FIG. 3. Composite linear/nonlinear calculation with the no-slip constraint imposed at all rational surfaces, and the natural frequencies in the absence of the RMP determined by the local $\mathbf{E} \times \mathbf{B}$ frequency. Top Panel: Full $n = 3$ vacuum island widths as functions of the least-squares linear fit to q_{95} versus time in DIII-D discharge #145380. Bottom Panel: Full $n = 3$ island widths as functions of time in DIII-D discharge #145380. The yellow, cyan, magenta, brown, pink, purple, and orange areas correspond to $m = 8$, 9, 10, 11, 12, 13, and 14, respectively. The yellow vertical bands indicate the ELM-suppression/mitigation windows. The horizontal dotted lines indicate the top of the pedestal, $\Psi_N = 0.925$.

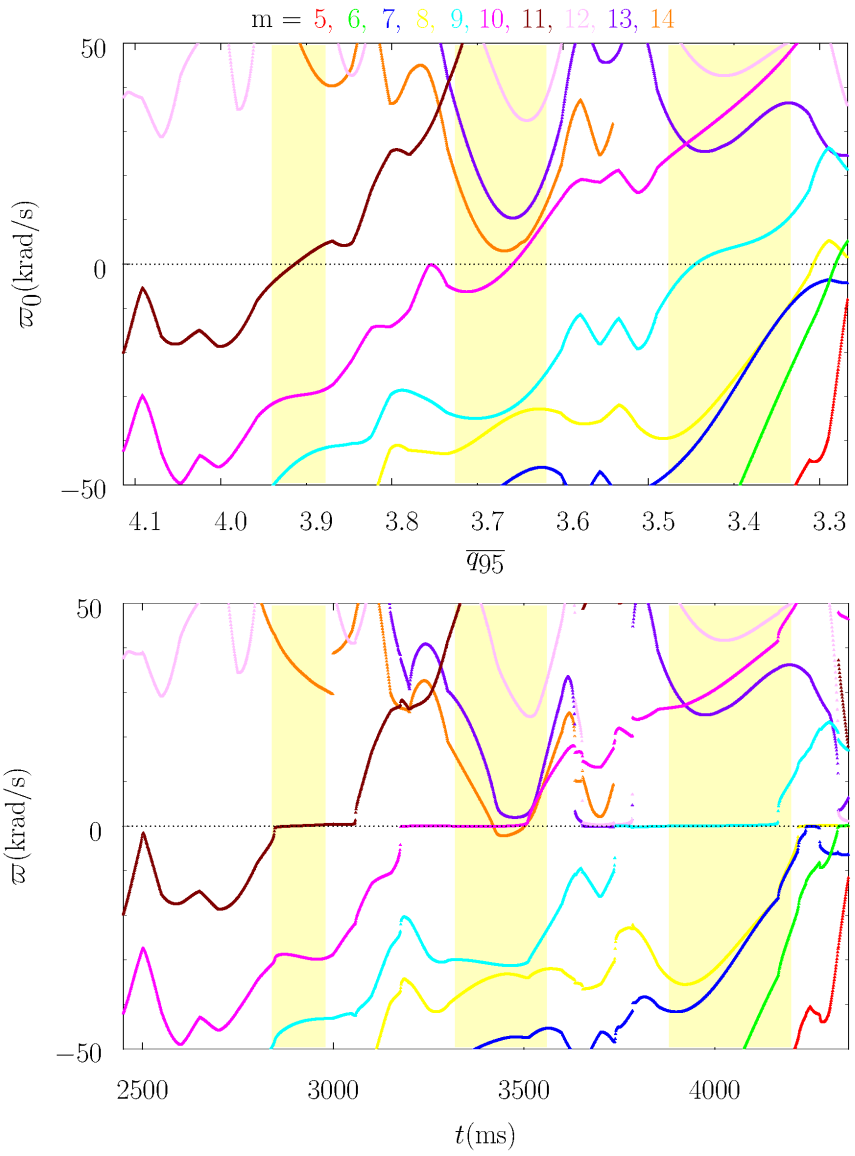

FIG. 4. Composite linear/nonlinear calculation with the no-slip constraint relaxed at all rational surfaces, and the natural frequencies in the absence of the RMP determined by the local $\mathbf{E} \times \mathbf{B}$ frequency. Top Panel: $n = 3$ natural frequencies, in absence of RMP, as functions of the least-squares linear fit to q_{95} versus time in DIII-D discharge #145380. Bottom Panel: $n = 3$ natural frequencies, in presence of RMP, as functions of time in DIII-D discharge #145380. The red, green, blue, yellow, cyan, magenta, brown, pink, purple, and orange curves correspond to $m = 5$, 6, 7, 8, 9, 10, 11, 12, 13, and 14, respectively. The yellow vertical bands indicate the ELM-suppression windows.

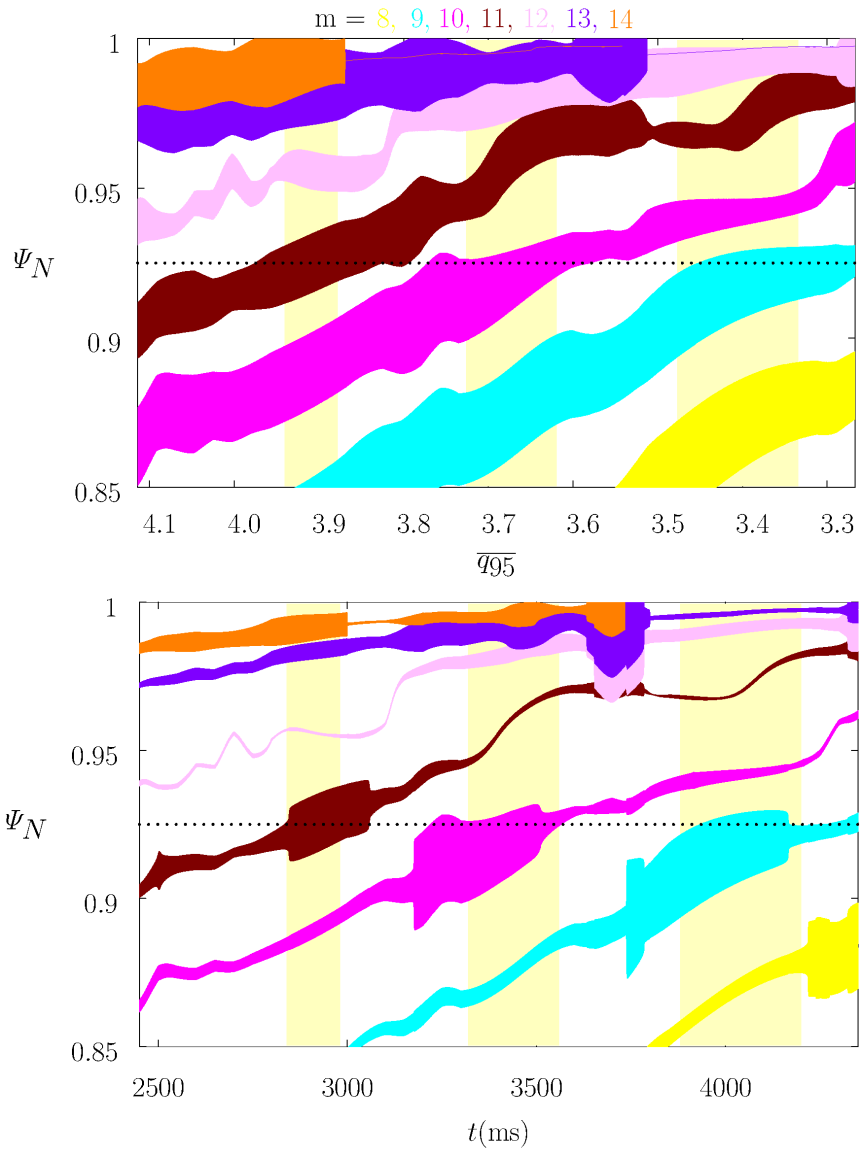

FIG. 5. Composite linear/nonlinear calculation with the no-slip constraint relaxed at all rational surfaces, and the natural frequencies in the absence of the RMP determined by the local $\mathbf{E} \times \mathbf{B}$ frequency. Top Panel: Full $n = 3$ vacuum island widths as functions of the least-squares linear fit to q_{95} versus time in DIII-D discharge #145380. Bottom Panel: Full $n = 3$ island widths as functions of time in DIII-D discharge #145380. The yellow, cyan, magenta, brown, pink, purple, and orange areas correspond to $m = 8$, 9, 10, 11, 12, 13, and 14, respectively. The yellow vertical bands indicate the ELM-suppression/mitigation windows. The horizontal dotted lines indicate the top of the pedestal, $\Psi_N = 0.925$.

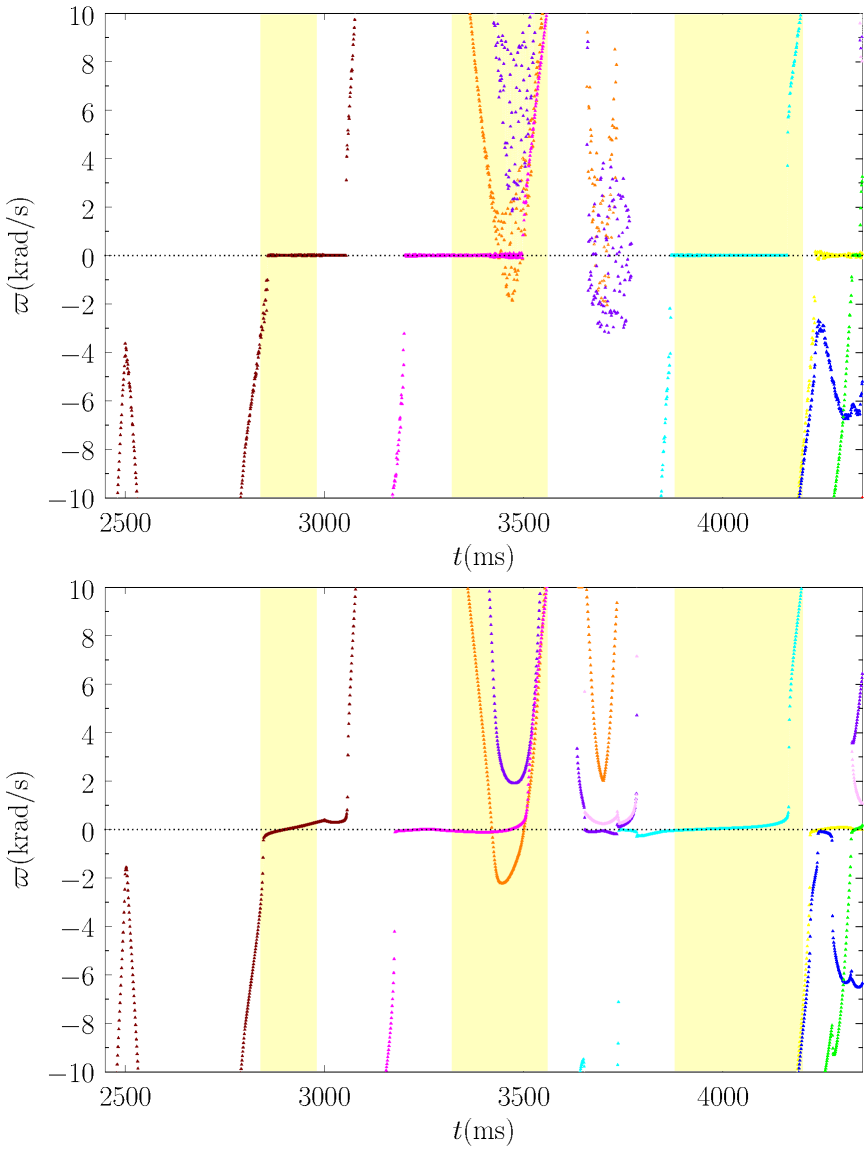

FIG. 6. Top Panel: Detail of the bottom panel of Fig. 2. Bottom Panel: Detail of the bottom panel of Fig. 4.

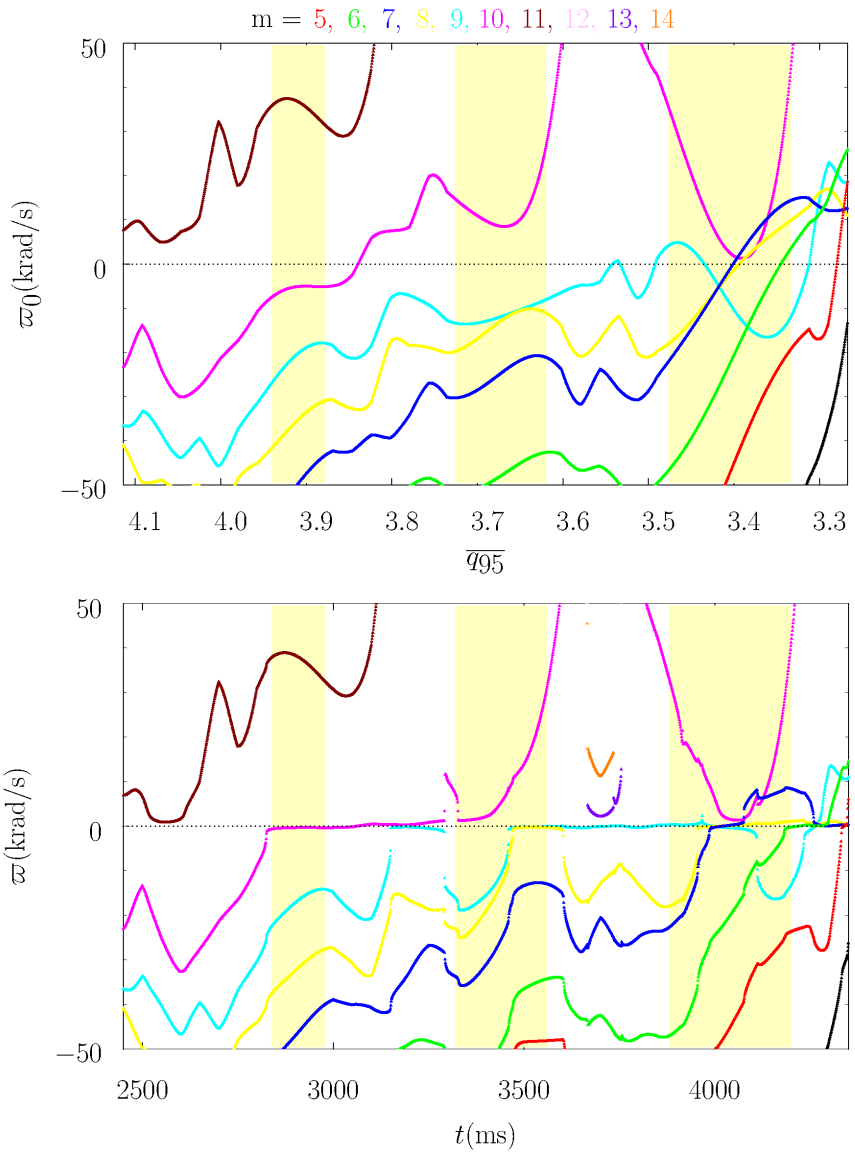

FIG. 7. Linear calculation with the no-slip constraint relaxed at all rational surfaces, and the natural frequencies in the absence of the RMP determined by linear theory. Top Panel: $n = 3$ natural frequencies, in absence of RMP, as functions of the least-squares linear fit to q_{95} versus time in DIII-D discharge #145380. Bottom Panel: $n = 3$ natural frequencies, in presence of RMP, as functions of time in DIII-D discharge #145380. The red, green, blue, yellow, cyan, magenta, brown, pink, purple, and orange curves correspond to $m = 5$, 6, 7, 8, 9, 10, 11, 12, 13, and 14, respectively. The yellow vertical bands indicate the ELM-suppression windows.

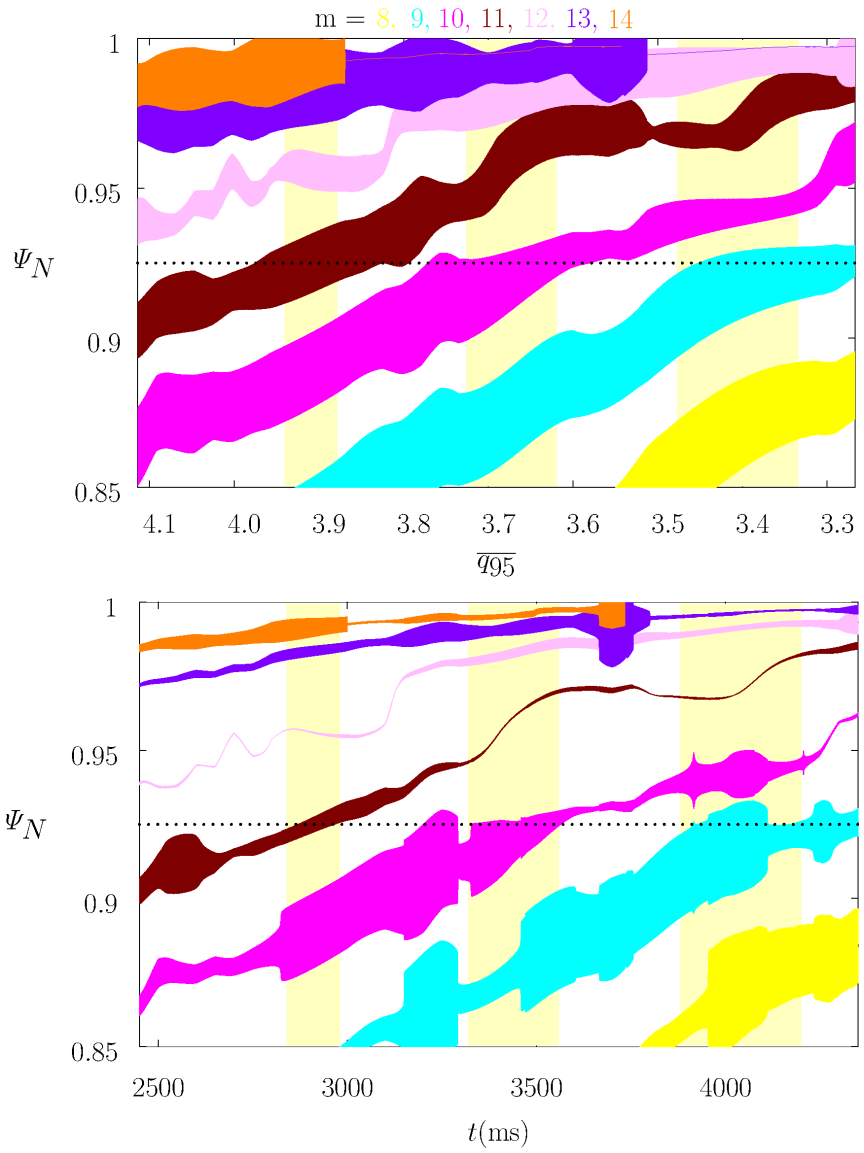

FIG. 8. Linear calculation with the no-slip constraint relaxed at all rational surfaces, and the natural frequencies in the absence of the RMP determined by linear theory. Top Panel: Full $n = 3$ vacuum island widths as functions of the least-squares linear fit to q_{95} versus time in DIII-D discharge #145380. Bottom Panel: Full $n = 3$ island widths as functions of time in DIII-D discharge #145380. The yellow, cyan, magenta, brown, pink, purple, and orange areas correspond to $m = 8$, 9, 10, 11, 12, 13, and 14, respectively. The yellow vertical bands indicate the ELM-suppression/mitigation windows. The horizontal dotted lines indicate the top of the pedestal, $\Psi_N = 0.925$.

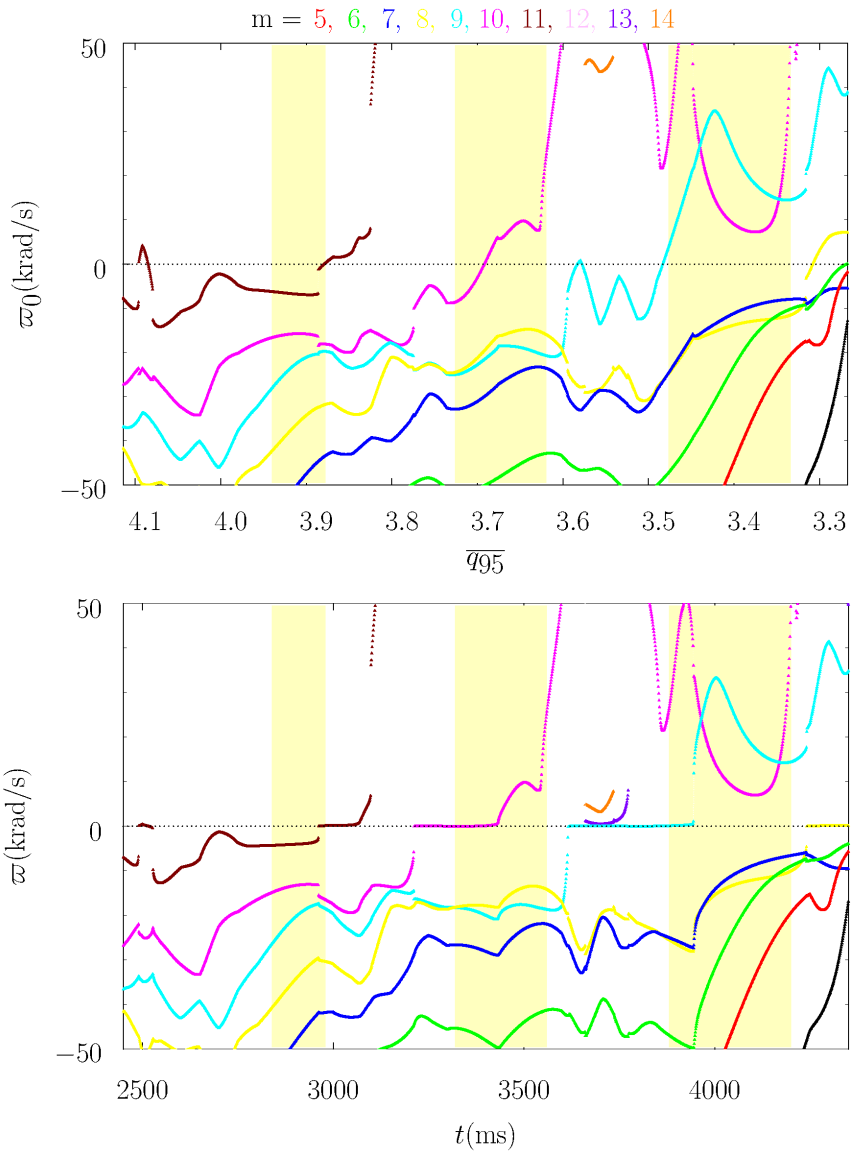

FIG. 9. Composite linear/nonlinear calculation with the no-slip constraint relaxed at all rational surfaces, and the natural frequencies in the absence of the RMP determined by composite linear/nonlinear theory. Top Panel: $n = 3$ natural frequencies, in absence of RMP, as functions of the least-squares linear fit to q_{95} versus time in DIII-D discharge #145380. Bottom Panel: $n = 3$ natural frequencies, in presence of RMP, as functions of time in DIII-D discharge #145380. The red, green, blue, yellow, cyan, magenta, brown, pink, purple, and orange curves correspond to $m = 5$, 6, 7, 8, 9, 10, 11, 12, 13, and 14, respectively. The yellow vertical bands indicate the ELM-suppression windows.

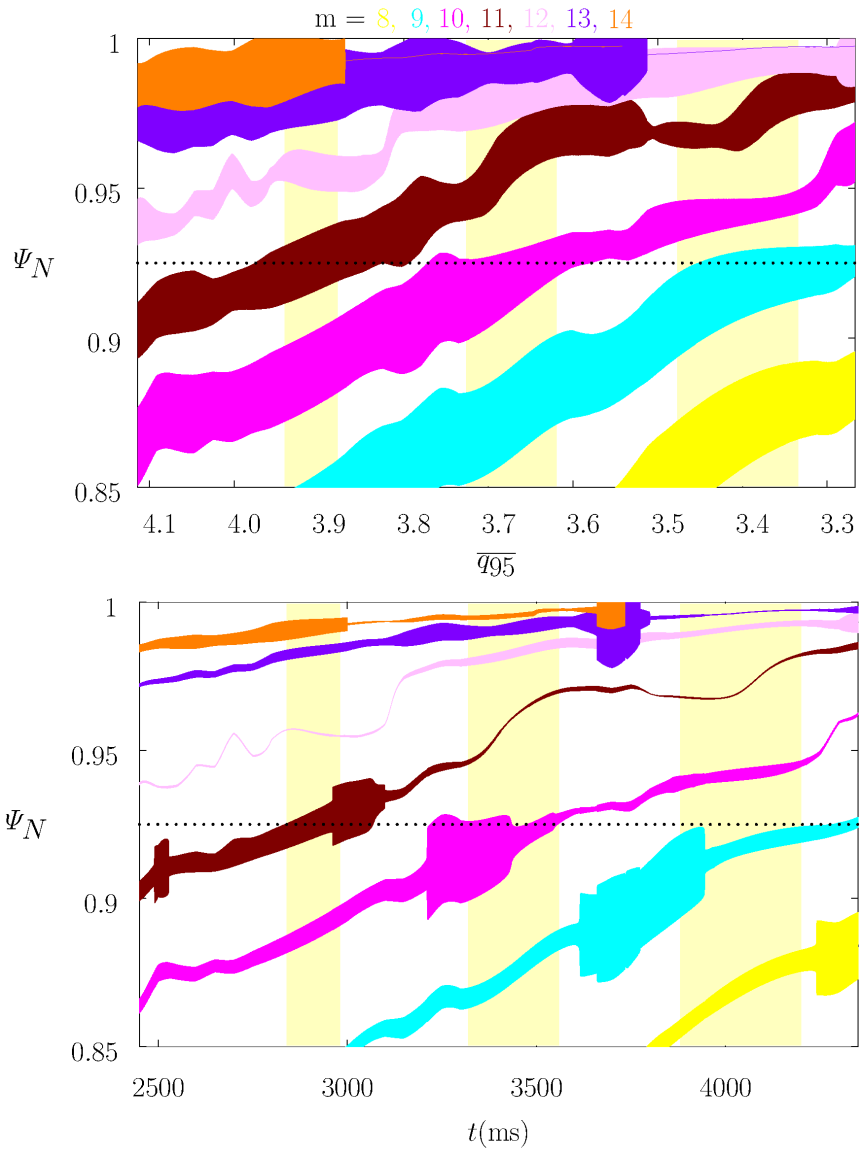

FIG. 10. Composite linear/nonlinear calculation with the no-slip constraint relaxed at all rational surfaces, and the natural frequencies in the absence of the RMP determined by composite linear/nonlinear theory. Top Panel: Full $n = 3$ vacuum island widths as functions of the least-squares linear fit to q_{95} versus time in DIII-D discharge #145380. Bottom Panel: Full $n = 3$ island widths as functions of time in DIII-D discharge #145380. The yellow, cyan, magenta, brown, pink, purple, and orange areas correspond to $m = 8$, 9, 10, 11, 12, 13, and 14, respectively. The yellow vertical bands indicate the ELM-suppression/mitigation windows. The horizontal dotted lines indicate the top of the pedestal, $\Psi_N = 0.925$.